Accepted Manuscript

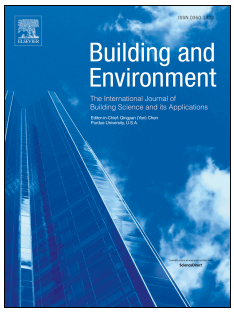

CFD simulations of near-field pollutant dispersion with different plume buoyancies

Yoshihide Tominaga, Ted Stathopoulos

PII: S0360-1323(18)30008-8

DOI: 10.1016/j.buildenv.2018.01.008

Reference: BAE 5244

To appear in: *Building and Environment*

Received Date: 29 October 2017

Revised Date: 2 January 2018

Accepted Date: 4 January 2018

Please cite this article as: Tominaga Y, Stathopoulos T, CFD simulations of near-field pollutant dispersion with different plume buoyancies, *Building and Environment* (2018), doi: 10.1016/j.buildenv.2018.01.008.

CFD Simulations of Near-field Pollutant Dispersion with Different Plume Buoyancies

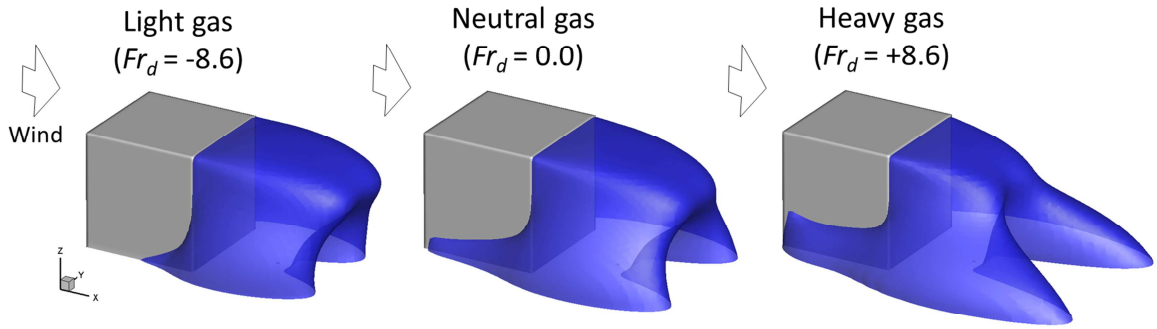

Iso-surface of concentration C/C_0=2.5

CFD Simulations of Near-field Pollutant Dispersion with Different Plume Buoyancies

Yoshihide Tominaga[a,] *, Ted Stathopoulos[b]

[a] Niigata Institute of Technology, Kashiwazaki, Japan
[b] Concordia University, Montreal, Canada

*Corresponding author: E-mail address: tominaga@abe.niit.ac.jp (Y. Tominaga).

Abstract

This study performs computational fluid dynamics simulations for flow and dispersion fields around an isolated cubic building model with tracer gases being exhausted from an exit behind the building. The tracer gases have three different buoyancies according to the difference in density with ambient air and, therefore, behave as neutral, light, and heavy gases. The performance of steady Reynolds-averaged Navier–Stokes (RANS) simulations with the Boussinesq approximation is examined herein by comparing the simulation results with the experimental results for different plume buoyancies. The steady RANS computations can generally reproduce the impact of plume buoyancy on the mean concentration in the experimental results even if the model performance for heavy gases is better than that for light gases and worse than that for neutral gases. This tendency is closely related to the prediction accuracy of the mean velocity and turbulent kinetic energy behind the building, which is restricted by the steady RANS simulations. The study also confirmed that the buoyancy modeling in the ε equation shows a negligible influence on the results.

Keywords:
CFD, Plume buoyancy, Near-field dispersion, Cubical building

1. Introduction

Predicting contaminant dispersion around buildings is one of the most important subjects in the fields of wind engineering and air conditioning engineering, among others. Many investigations have been performed using wind tunnel tests to predict pollutant dispersion around buildings [1]. However, wind tunnel tests encounter several difficulties, and have many limitations in analyzing the extremely complicated turbulent diffusion process around buildings located in atmospheric boundary layers. One of these difficulties is the buoyancy treatment in dispersed pollutants. The existence of negative or positive buoyancies in pollutants largely influences flow and dispersion fields [2, 3]. However, the similarity criteria for modeling dispersed pollutants with buoyancy have become considerably complicated [4–6]. Numerical methods based on computational fluid dynamics (CFD) could possibly overcome this difficulty and facilitate the precise investigation of the effect of buoyancy on flow and dispersion fields.

As reviewed by several papers [1, 7–12], a considerable amount of research has used the CFD technique to investigate pollutant dispersion around buildings. However, most of these studies treated tracer gases as neutrally buoyant (passive) scalars [13–18]. A few examples of these CFD studies on near-field dispersion explicitly considered pollutant buoyancy. In previous studies, light gases were often treated as thermal plumes with positive buoyancy [19–22]. Demuren and Rodi [19] presented a pioneering CFD study of the flow and temperature field past cooling towers using a simple buoyancy-extended k–ε model. They found that the most important features, namely the complex flow pattern in the immediate vicinity of the tower and the downwash as strong cross winds, the formation and decay of longitudinal vortices, and the trajectory and spreading of the plume under various conditions, were simulated reasonably well. However, it was pointed out that the lifting effect of the buoyancy on the plume in the initial region was under-predicted because of the excessive mixing, which was caused partly by an inaccurate numerical solution (numerical diffusion) and partly by the turbulence model. Olvera et al. [21] conducted a CFD study with a renormalization group (RNG) k–ε model to estimate the effects of the positive buoyancy on the flow structure and the dispersion characteristics inside the recirculation cavity region with different gas densities and exit velocities. Although they concluded that plume buoyancy could cause considerable flow disturbances by expanding the velocity defect

to greater heights and changing the cavity size and shape and flow direction, particularly inside the wake region, the prediction accuracy of the flow and concentration fields was not sufficiently validated in their study. Meanwhile, heavy gases, such as liquefied natural gas (LNG), have been treated in near-field dispersion studies as dense gases with a negative buoyancy [23–27]. Gavelli et al. [24] discussed the critical parameters necessary for a CFD model to accurately predict the behavior of an LNG spill in a geometrically complex domain by comparing the gas concentrations measured by experiments with those predicted by CFD using the Reynolds stress model. The study revealed that an accurate representation of the LNG spill required not only knowledge of the mass flow and evaporation rates, but also an estimate of the velocity at which the LNG is spilled and evaporated. Scargiali et al. [25] presented a CFD simulation strategy with the standard k–ε model for modeling dense cloud dispersion in urban environments. It was confirmed that increasing the amount of heavy gas released showed down the cloud and increased the maximum concentrations and the lateral spread of the cloud caused by larger negative buoyancy effects. However, the effect was not quantitatively examined. Furthermore, very few studies analyzed light and heavy gases simultaneously. Ohba et al. [28] conducted a validation study of the CFD models for heavy and light gas dispersion discharged from a storage tank. Diffusion patterns for the heavy, light, and neutral gases changed due to the gravitational effect on dispersion (i.e., heavy gas diffused upwind and in lateral directions like a drainage flow, whereas light gas diffused upward like a plume from a stack). However, the quantitative evaluation of the model performance was not considered for the predicted results, including the velocity field.

As mentioned earlier, although several studies for buoyant gas dispersion around building structures have been reported in the literature, very few studies (i) systematically analyzed the effect of the plume buoyancy on the turbulent flow and concentration fields, (ii) treated positive and negative buoyancies simultaneously, and (iii) validated the CFD method by experimental data quantitatively. The present study performs CFD simulations for flow and dispersion fields around an isolated cubic building model with tracer gases being exhausted from an exit behind the building. The tracer gases are treated as neutral, light, and heavy gases according to the density differences with ambient air. The Reynolds-averaged Navier–Stokes (RANS) simulations with the Boussinesq approximation are used to investigate the effect of

pollutant buoyancies on the prediction accuracy by comparing the simulation results with the wind tunnel experiment results. As it is well known, the approximation is accurate as long as changes in the actual density are small ($|\Delta\rho/\rho_a| \ll 1$) [30]. However, the treating flow and dispersion field have buoyant plumes with $|\Delta\rho/\rho_a| = 0.7$. Therefore, the applicability of the Boussinesq approximation for this type of near-field dispersion should be confirmed. Then, the effect of plume buoyancy on flow and concentration fields is investigated. Unsteady approaches such as unsteady RANS [31], large-eddy simulation (LES) [16, 17], and detached-eddy simulation (DES) [32], may provide more precise prediction results. However, considering the lack of previous studies on near-field dispersion with different plume buoyancies regardless of turbulence models, steady RANS is used herein as the most practical approach to provide insight into the applicability of CFD to such a dispersion field.

2. Flow and dispersion fields

2.1 Target configuration

The target configuration is determined based on the experiments reported by Tominaga et al. [33, 34]. Figure 1 illustrates the analyzed flow situation. A cubic building model with height H is located in the turbulent boundary layer. A square-shaped gas source with a $0.025H$ side length is set at the ground level in the recirculation region behind the building. The exit gas speed W_S is $0.5U_H$, with U_H defined as the upwind mean velocity at height H. Table 1 lists the cases compared in this study. The densimetric Froude numbers Fr_d defined by Eq. (1) are determined, such that their absolute values are identical for the light and heavy gases.

$$Fr_d = \frac{g\Delta\rho H}{\rho_a U_H^2}, \qquad (1)$$

where ρ_a is the ambient air density; ρ_s is the gas density; $\Delta\rho$ is determined as $\rho_a - \rho_s$; and g is the gravitational acceleration (-9.8 m/s^2).

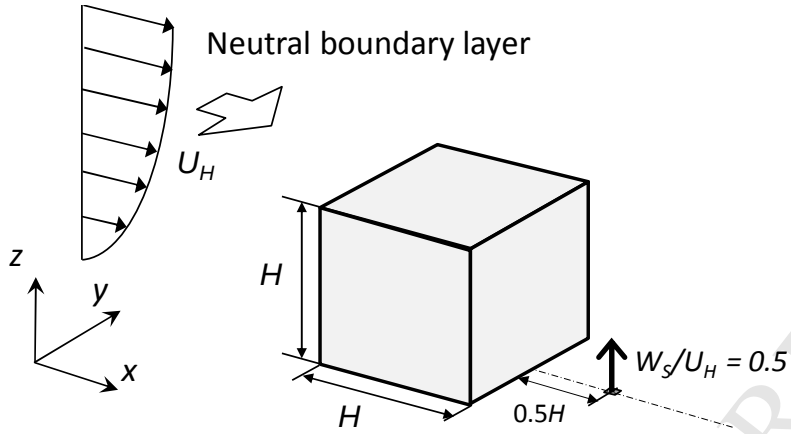

Figure 1. Model flow field.

Table 1. Investigated cases.

Case	ρ_s/ρ_a	$\Delta\rho/\rho_a$	Fr_d
Neutral gas	1.0	0	0.0
Light gas	0.3	−0.7	−8.6
Heavy gas	1.7	+0.7	+8.6

2.2 Experimental setup

The experiments were performed in a boundary layer wind tunnel at the Institute of Industrial Science in the University of Tokyo [33, 34]. The H and U_H values were 0.2 m and 0.4 m/s, respectively. The power law exponent of the vertical profile of the inflow velocity was 0.25. The streamwise turbulence intensity at building height H was approximately 20%. Figure 2 shows the incident vertical profiles of the dimensionless mean velocity U/U_H and the turbulence intensity $I_u = (\sqrt{\overline{u'^2}}/U)$ (those measured at the center of the turntable without the building model, which is the origin of all the measurements). The Reynolds number (Re) based on U_H and H was 5.7×10^3. By comparing the results with those for $Re = 5.7 \times 10^4$, the preliminary experiments confirmed that the effect of the Re was very small.

The concentration measurements were performed using a high-speed total hydrocarbon analyzer (HFR300, Cambustion Limited). C_2H_4 was used as a neutral tracer gas. A mixture of He and C_2H_4 and that of SF_6 and C_2H_4 were used as the light and heavy gases, respectively, to consider the negative and positive buoyancies listed in

Table 1. All concentrations in this study are expressed in non-dimensional form. The non-dimensional concentration C^* is defined as follows:

$$C^* = \frac{C}{c_0}, \qquad (2)$$

where c_0 is the reference concentration expressed as:

$$c_0 = \frac{Q_e}{H^2 U_H}, \qquad (3)$$

where Q_e is the pollutant exhaust rate.

The pollutant exhaust rate Q_e in eq. (3) is defined as the volume flow rate that includes not only C_2H_4 but also He and SF_6. Therefore, the mass flow rate differs for pollutants with different densities. However, it is reasonable to use this reference concentration to discuss the influence of the change in plume density, because the concentration was calculated as volume concentration by measuring the output ratio of the sampling gas to the span gas including the diluents. The value of c_0 was 312.5 ppm in the experiments.

The wind velocity was measured using a tandem-type hot wire anemometer, which can discern the three-dimensional components of a velocity vector. The heat transfer from the hot wire is proportional to the Nusselt number, which is related to the fluid density. Therefore, the measured wind velocity might have some influence on the density of the measuring fluid. However, because the areas affected by the different plume densities are limited only to the upwind region from the gas exit, this influence was neglected, as will be discussed later in the paper. The sampling frequency was set to 10 Hz to obtain 4,096 data points for each measurement point.

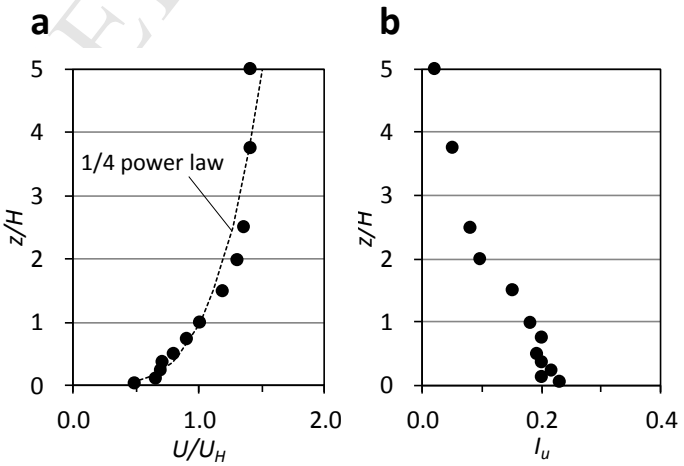

Figure 2. Incident profiles of the (a) mean streamwise dimensionless velocity U/U_H and (b) turbulence intensity I_u.

3. Computational setup

3.1 Numerical methods

The commercial software ANSYS FLUENT 16.0 is used for the steady RANS computations based on a control volume approach for solving flow and mass fraction equations [34]. Incompressible flow under the Boussinesq approximation, which treats density as a constant value in all solved equations, except for the buoyancy term in the momentum equation, has been considered. This approximation is accurate as long as changes in the actual density are small ($|\Delta\rho/\rho_a| \ll 1$) [35]. In this study, $\Delta\rho/\rho_a$ is ± 0.7 for the buoyant gases; therefore, the difference in density is greater than the suggested upper bound of the Boussinesq approximation [36]. To confirm the applicability of the Boussinesq approximation for this type of near-field dispersion is one of the objectives of the study.

The Green–Gauss cell based scheme is used for gradient discretization. The advection terms are discretized using a second-order upwind scheme [34]. The semi-implicit method for the pressure-linked equation (SIMPLE) algorithm is used for the pressure–velocity coupling [37].

The local mass fraction of the species, Φ_s, is predicted by solving a convection-diffusion equation for the species:

$$\frac{\partial}{\partial t}(\rho\Phi_s) + \frac{\partial}{\partial x_i}(\rho\Phi_s U_i) = \frac{\partial}{\partial x_j}\left(\rho D \frac{\partial \Phi_s}{\partial x_j} - \overline{u_j{}'\Phi_s{}'}\right) \qquad (4)$$

Here, D is the mass diffusion coefficient for the species in the mixture, and μ_t is the turbulent viscosity.

The mass fraction Φ_s can be converted to volume concentration C by using the following relationship:

$$\Phi_s = \frac{C\cdot\rho_s}{C\cdot\rho_s + (1-C)\cdot\rho_a} \qquad (5)$$

where ρ_a is the ambient air density and ρ_s is the gas density.

3.2 Domain, computational grid, and boundary conditions

The boundary conditions are set by following basic available guidelines [38, 39]. The computational domain covers a volume of 21.0H (x) × 9.7H (y) × 5.4H (z) and the

distance between the windward face of the cube and domain inlet is 5.0*H* (Figure 3). The domain is discretized into 1,072,080 hexahedral grids based on the preliminary grid sensitivity studies outlined in Section 4.1.

The vertical distributions of the streamwise mean velocity U and turbulent kinetic energy k are given by using the experimental data as interpolated values of approximation curves (cf. Figure 2). The turbulent kinetic energy k is calculated from the mean wind velocity U and the longitudinal turbulence intensity I_u using Eq. (4), where $a = 1$ is chosen as recommended by Tominaga et al. [39].

$$k(z) = a(I_u(z)U(z))^2 \tag{6}$$

The ε values are determined based on the assumption of the local equilibrium $P_k = \varepsilon$, where P_k is the production term in the k equation. For the ground surface, the wall functions are modified according to the roughness specified by an equivalent sand–grain roughness height k_s and a roughness constant C_S. k_s is defined using the function proposed by Blocken et al. [40], i.e. $k_s = 9.793z_0/C_S$, in which z_0 is estimated to be 0.0004 m by the velocity profile obtained from the experiments and *Cs* is taken as 0.5. The turbulence intensity of the exhaust outlet velocity is set to 10%.

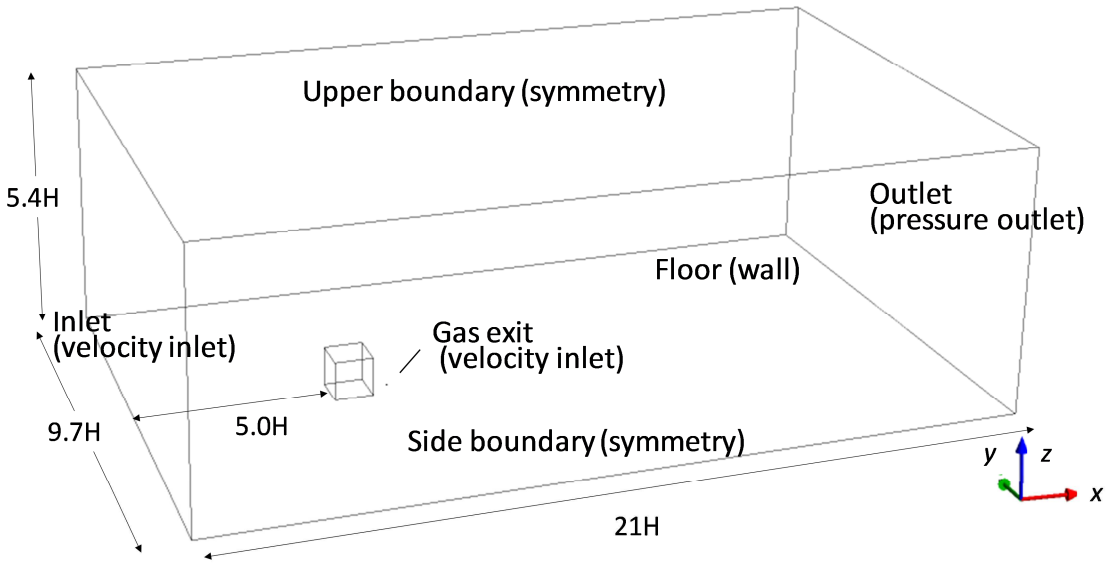

Figure 3. Computational domain and boundary conditions.

3.3 Turbulence models

Four types of turbulence models are used and compared, namely the standard k–ε model (SKE) [41], RNG k–ε model (RNG) [42], realizable k–ε model (RLZ) [43], and shear stress transport (SST) k–ω model (SST) [44]. All model constants are set to their default values in the software.

The k–ε models in the software account for the generation of k when a non-zero gravity field and a density gradient are simultaneously present, as in the case of this study, because of buoyancy G_b:

$$G_b = -g\frac{\mu_t}{\rho Pr_t}\frac{\partial \rho}{\partial z}, \qquad (7)$$

where Pr_t is the turbulent Prandtl number for energy (0.85 is used as the default value [34]). This means that the turbulent kinetic energy tends to be augmented ($G_b > 0$) for an unstable stratification ($\frac{\partial \rho}{\partial z} > 0$), and buoyancy tends to suppress the turbulence ($G_b < 0$) for a stable stratification ($\frac{\partial \rho}{\partial z} < 0$).

The effects of the buoyancy on the generation of k were relatively well understood. However, its effect on ε was less clear [34]. The transport equation for ε is expressed as follows:

$$\frac{\partial}{\partial t}(\rho\varepsilon) + \frac{\partial}{\partial x_i}(\rho\varepsilon U_i) = \frac{\partial}{\partial x_j}\left[\left(\mu + \frac{\mu_t}{\sigma_\varepsilon}\right)\frac{\partial \varepsilon}{\partial x_j}\right] + C_{1\varepsilon}\frac{\varepsilon}{k}(G_k + C_{3\varepsilon}G_b) - C_{2\varepsilon}\frac{\varepsilon^2}{k} \qquad (8)$$

where G_k is the shear production of k. The degree to which ε is affected by the buoyancy is determined by the constant $C_{3\varepsilon}$. As reviewed by Kumar and Dewan [45], the modeling approach of this effect was historically discussed in the mechanical engineering field, but was less discussed in the wind engineering and building environmental fields. By default, in the software, the effects of buoyancy on ε are simply neglected by setting $C_{3\varepsilon}$ to zero. However, optionally, $C_{3\varepsilon}$ is calculated according to the following relationship [34]:

$$C_{3\varepsilon} = tanh\left|\frac{\boldsymbol{v}}{\boldsymbol{u}}\right|, \qquad (9)$$

where $\boldsymbol{v}$ and $\boldsymbol{u}$ are the components of the flow velocity parallel and perpendicular to the gravitational vector, respectively. $C_{3\varepsilon}$ will become 1 for buoyant shear layers, in which the main flow direction is aligned with the direction of gravity; and $C_{3\varepsilon}$ will become

zero for the buoyant shear layers perpendicular to the gravitational vector. Meanwhile, Viollet [46] proposed a $C_{3\varepsilon}$ treatment, in which its values are switched according to the sign of the density gradient:

$$C_{3\varepsilon} = \begin{cases} 1.0\ (G_b > 0) \\ 0\ (G_b \leq 0) \end{cases}. \qquad (10)$$

Section 5 presents the impact of the $C_{3\varepsilon}$ treatment on the results.

The turbulent mass flux in eq. (4) is modeled by the standard gradient diffusion hypothesis:

$$-\overline{u_j'\phi_s'} = \frac{\mu_t}{Sc_t}\frac{\partial \Phi_s}{\partial x_j} \qquad (11)$$

The turbulent Schmidt number Sc_t for the reference case is set to 0.7 as the default value in the software (see Tominaga and Stathopoulos [47]). Sections 4.3 and 5.3 present the sensitivity of Sc_t to the model performance.

3.4 Validation metrics

The following validation metrics are used to quantify the agreement between the computational and experimental results [48]: the fraction of the prediction within a factor of 2 of the observations (FAC2), fractional bias (FB), and normalized mean square error (NMSE). These metrics can be expressed as follows:

$$FAC2 = \frac{1}{N}\sum_{i=1}^{N} n_i \ with\ n_i = \begin{cases} 1\ for\ 0.5 \leq \frac{P_i}{O_i} \leq 2 \\ 1\ for\ O_i \leq W\ and\ P_i \leq W \\ 0\ else \end{cases} \qquad (12)$$

$$FB = \frac{[O]-[P]}{0.5([O]+[P])} \qquad (13)$$

$$NMSE = \frac{[(O_i-P_i)^2]}{[O][P]}, \qquad (14)$$

where O_i and P_i are the observed (measured) and predicted (computed) values of a given variable for sample i, respectively; and N is the number of data points. The square brackets denote the average over the entire dataset. The allowed absolute difference W is set to 0.05 for FAC2. The ideal values of the metrics corresponding to the perfect agreement are 1.0 for FAC2 and 0 for the FB and NMSE. Although other validation metrics such as geometric mean bias (MG) and geometric variance (VG) are also available, it is sufficient to check the above three metrics as typically representative. Previous studies suggested the following judgment criteria for these metrics for

concentration: FAC2 > 0.5, |FB| < 0.3, NMSE < 4 [48, 49]. In the present study, the metrics for the mean concentration consider 55, 68, and 61 measurement points on the vertical plane (y = 0) and 40, 49, and 40 points on the horizontal plane (z = 0) for the neutral, light, and heavy gases, respectively.

4. Results for neutral gas

4.1 Impact of the computational grid resolution

A grid-sensitivity analysis is performed based on two additional grids: a coarser grid and a finer grid. As mentioned earlier, the basic grid had 1,072,080 cells, where each building side is assigned 23 cells. Each side of the square-shaped gas exit is assigned with five cells. The coarser grid had 428,707 cells, while the finer grid had 2,626,767 cells, where each side of the gas exit was assigned with three and seven cells each. The realizable k–ε model was adopted as the turbulence model. Figure 4 shows the outlines of the three grids. Figure 5 depicts a comparison of the results for the mean concentration on the three grids. A small deviation is found among the three grids for the lower part of the line at x/H = 0.55 and between the basic and coarse grids for the other two lines at x/H = 1.0 and 1.5, respectively. No significant grid sensitivity was found for the other parts. Therefore, the resolutions of the vicinity of the building and the gas exit adopted in the basic grid are retained for the other cases.

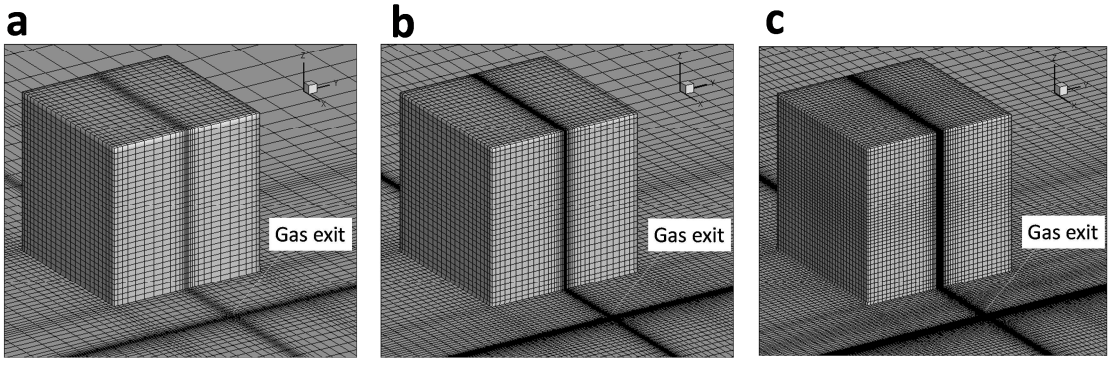

Figure 4. Computational grids for the grid-sensitivity analysis: (a) coarse grid, (b) basic grid, and (c) fine grid.

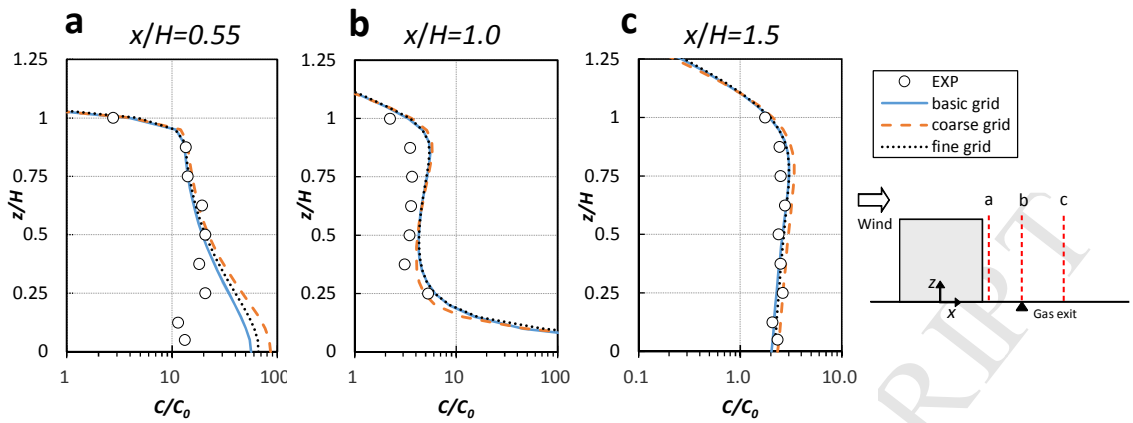

Figure 5. Grid-sensitivity analysis results: mean concentration C/C_0 values along the three vertical lines at a center section: (a) x/H = 0.55, (b) x/H = 1.0, and (c) x/H = 1.5.

4.2 Impact of the turbulence models

Figure 6 compares the vertical profiles of the mean streamwise velocities U/U_H behind the building by CFD with the four turbulence models, i.e., the standard k–ε model (SKE), RNG k–ε model (RNG), realizable k–ε model (RLZ), and shear stress transport (SST) k–ω model (SST), and the experiment. The prediction results, except those of the k–ω SST model, are quite similar and generally close to the experimental results. However, all the computational results show a strong reverse flow at x/H = 2.0. The strongest recirculation flows are predicted by k–ω SST, while the weakest is by the SKE. Large recirculation flows occur behind the building mainly because the periodic velocity fluctuation behind the building is not reproduced in the steady RANS computation, as indicated in previous studies [50].

Figure 7 compares the vertical and horizontal profiles of the mean concentrations behind the building. As regards the velocity distributions at the vertical lines (Figure 6), except for the k–ω SST, no significant difference is found in the general distributions among the other three turbulence models, which well reproduced the concentration distributions in the experiment. The RNG k–ε and k–ω SST models at the horizontal lines show a larger concentration transport in the lateral direction than the other models and the experiment at x/H = 1.0 and 1.5. Table 2 lists the validation metrics described in Section 3.4 for the mean concentrations. The realizable k–ε model provides the best agreement with the experimental data in terms of the mean concentrations. Therefore,

the realizable k–ε model is used as the representative turbulence model for Section 4.3 and Section 5.

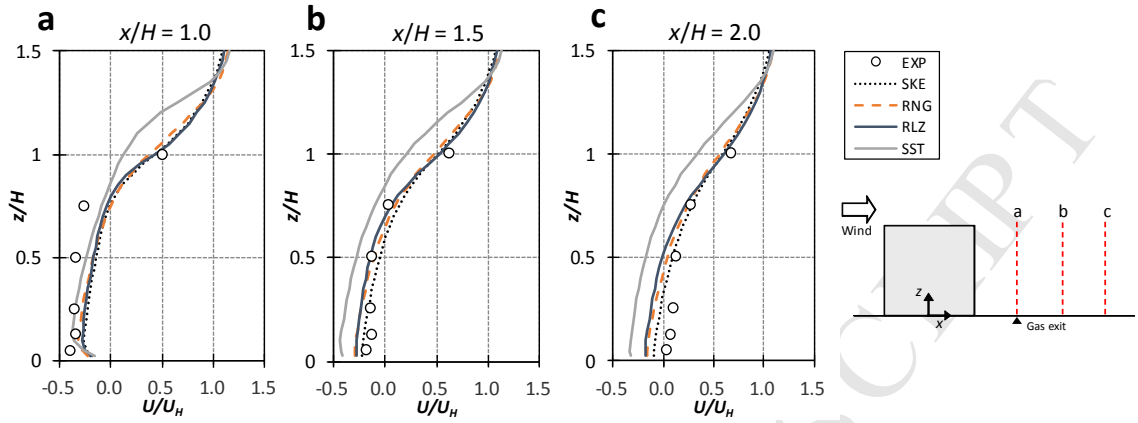

Figure 6. Vertical profiles of the mean streamwise velocity U/U_H at the center section behind the building obtained by various turbulence models: (a) x/H = 1.0, (b) x/H = 1.5, and (c) x/H = 2.0.

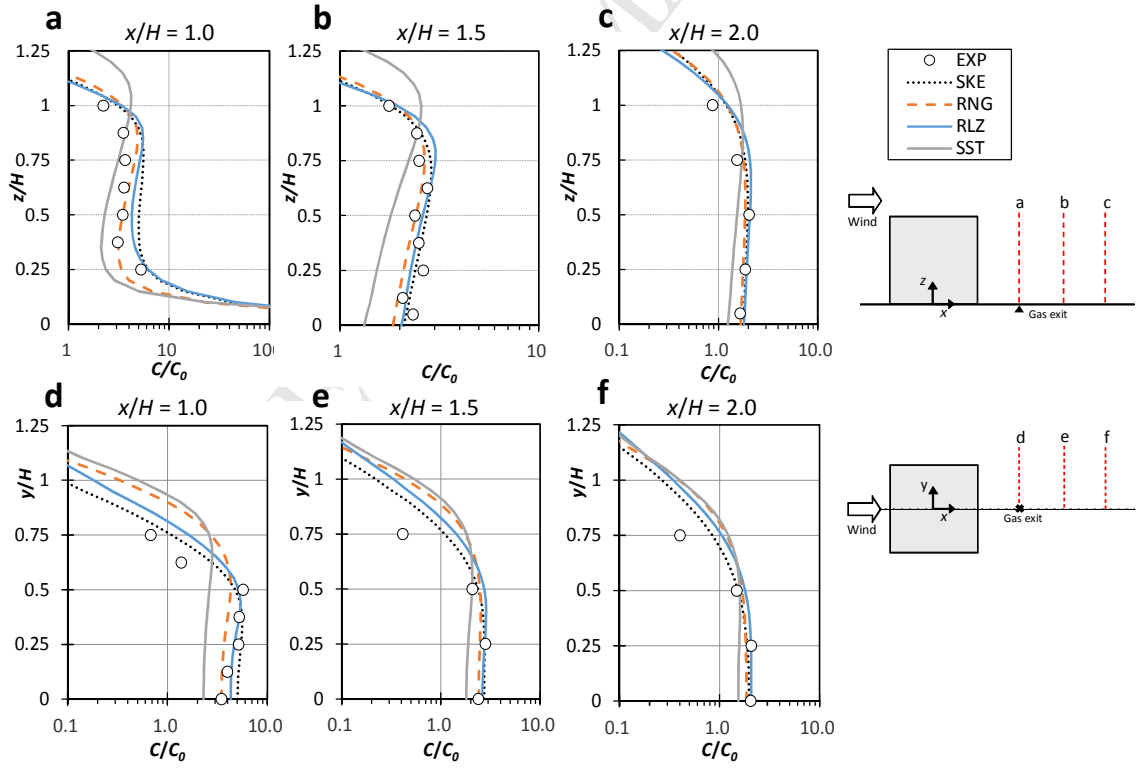

Figure 7. Profiles of the mean concentrations C/C_0 behind the building obtained by various turbulence models: (a–c) vertical profiles at a center section (y/H = 0) and (d–f) horizontal profiles at a half building height (z/H = 0.5).

Table 2. Validation metrics for the mean concentration C/C_0.

	FAC2	FB	NMSE
Standard k–ε	0.89	−0.39	4.61
RNG k–ε	0.82	−0.41	6.49
Realizable k–ε	0.87	−0.30	2.82
k–ω SST	0.72	−0.25	4.77

4.3 Impact of the turbulent Schmidt number

Figure 8 compares the vertical and horizontal profiles of the mean concentrations behind the building with different turbulent Schmidt numbers: Sc_t = 0.3, 0.7 (reference case) and 1.1. The case with Sc_t = 0.7 at the vertical lines indicates a generally good agreement with the experiment results. The concentrations at x/H = 1.5 and 2.0 are underestimated by the case with Sc_t = 0.3 and overestimated by the case with Sc_t = 1.1. Meanwhile, the concentrations in the building wake (y/H < 0.5) at the horizontal lines at x/H = 1.0 and 1.5 are overestimated by all the cases. This overestimation is improved by the case with Sc_t = 0.3. However, the concentrations seem to be overestimated outside of the building wake. As a well-known tendency, the steady RANS simulations show that the smaller Sc_t provides better results in general distributions of the concentration, especially at the high concentration region [51, 52], because the underestimation of the turbulent diffusion in the steady RANS computation caused by the lack of large-scale unsteady fluctuations behind the building is compensated by the smaller Sc_t. However, note that the concentrations are overestimated at the area far from the high concentration region near the source.

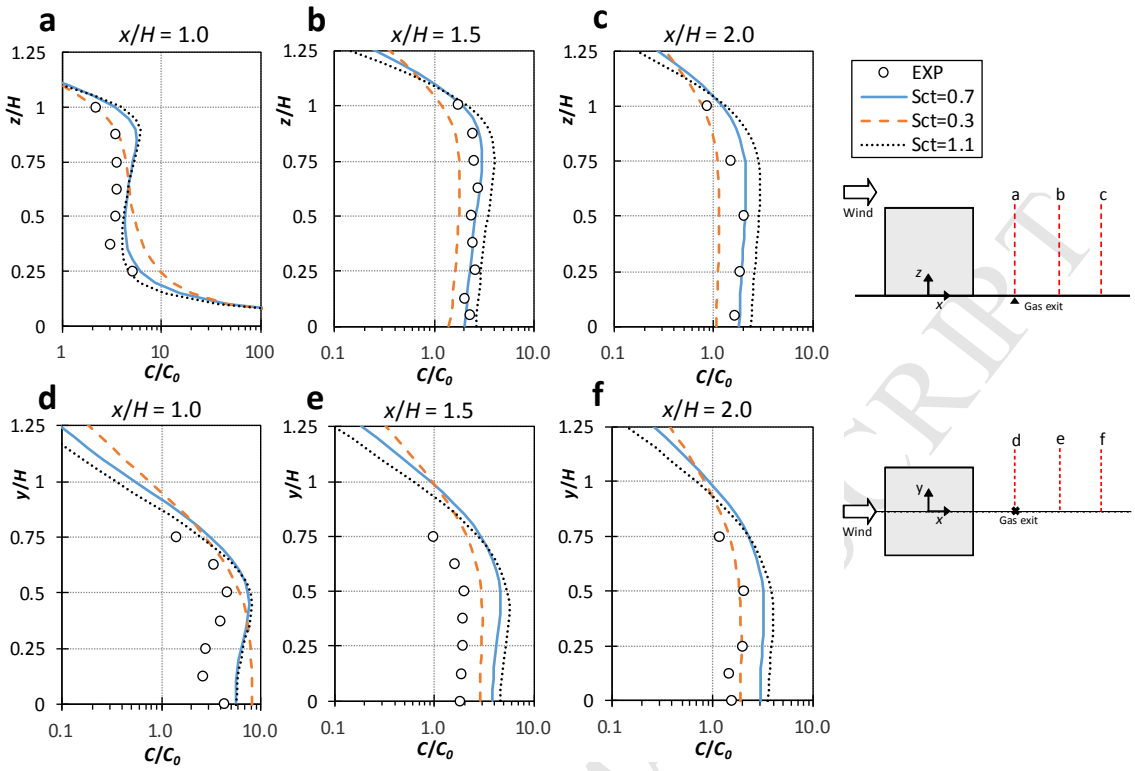

Figure 8. Profiles of the mean concentration C/C_0 behind the building obtained with different turbulent Schmidt numbers: (a–c) vertical profiles at the center section (y/H = 0) and (d–f) horizontal profiles at a half building height (z/H = 0.5).

5. Results for the buoyant gases

5.1 Impact of the plume buoyancies on the velocity and the turbulence fields

Figure 9 compares the predicted distributions of fluid density for the buoyant gases. The areas prominently affected by the different plume densities are limited only to the upwind region from the gas exit. The plume of the heavy gas spreads lower than that of the light gas. Figure 10 illustrates the streamlines and the contours of the vertical component of the velocity at the center section with different plume buoyancies. The effect of the plume buoyancies on the general velocity field is not very large. However, the vertical component of the velocity in the wake region is larger for the light gas than for the neutral and heavy gases. A slightly negative value of the vertical velocity is observed between the gas exit and the back of the building for the heavy gas. Figure 11 shows the contours of the turbulent kinetic energy k at the center section with different

plume buoyancies. Only *k* values near the gas exit are affected by the plume buoyancy. In the light (heavy) gas case, the value of *k* is much larger (smaller) than the neutral gas. Figure 12 compares the vertical distributions of the turbulent kinetic energy *k* with different plume buoyancies near the source position. The computational results for all gases successfully reproduced the tendency of the buoyancy effect on the turbulent kinetic energy, as explained in Section 3.3 (i.e., the light gas shows a larger value, while the heavy gas shows smaller values compared to those of the neutral gas). However, their predicted values are overestimated compared to those of the experiment.

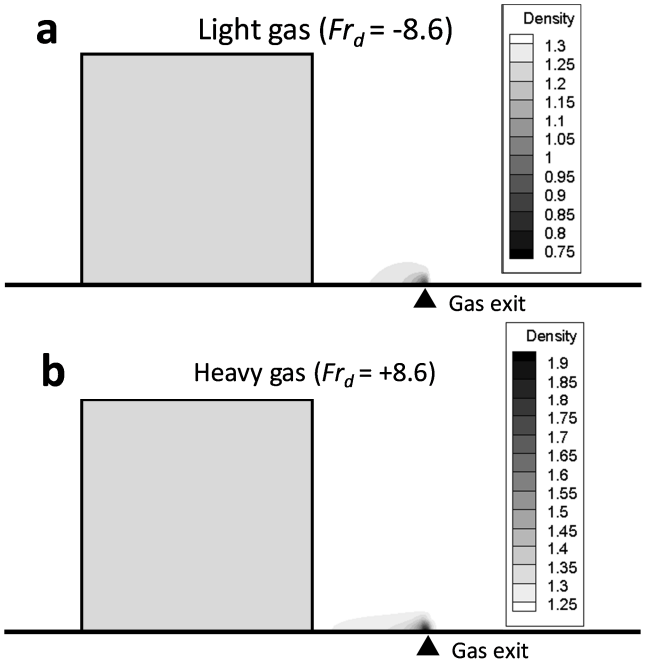

Figure 9. Fluid density at the center section with different plume buoyancies: (a) light gas, (b) heavy gas.

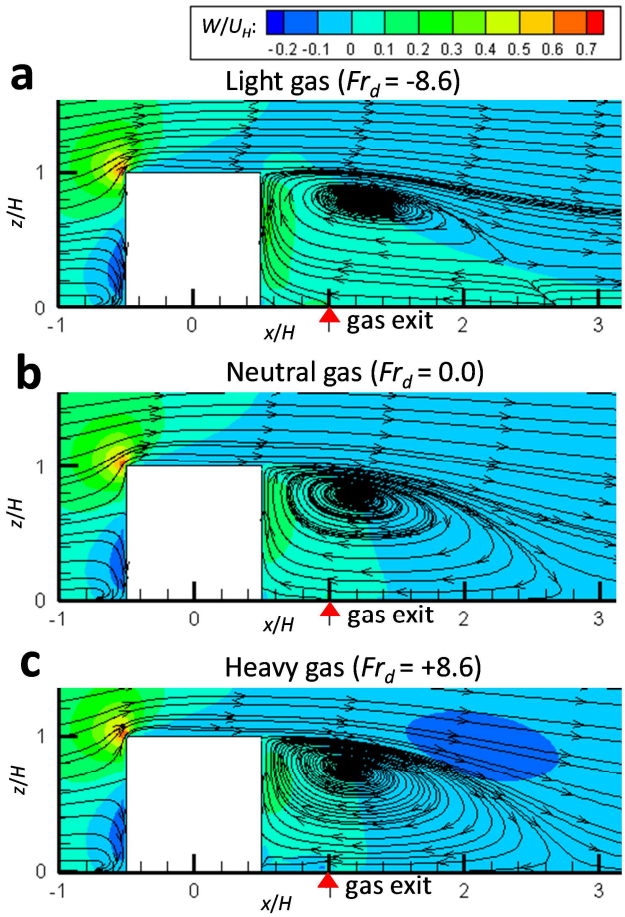

Figure 10. Streamlines and contours of the vertical component of the velocity W/U_H at the center section with different plume buoyancies: (a) light gas, (b) neutral gas, and (c) heavy gas.

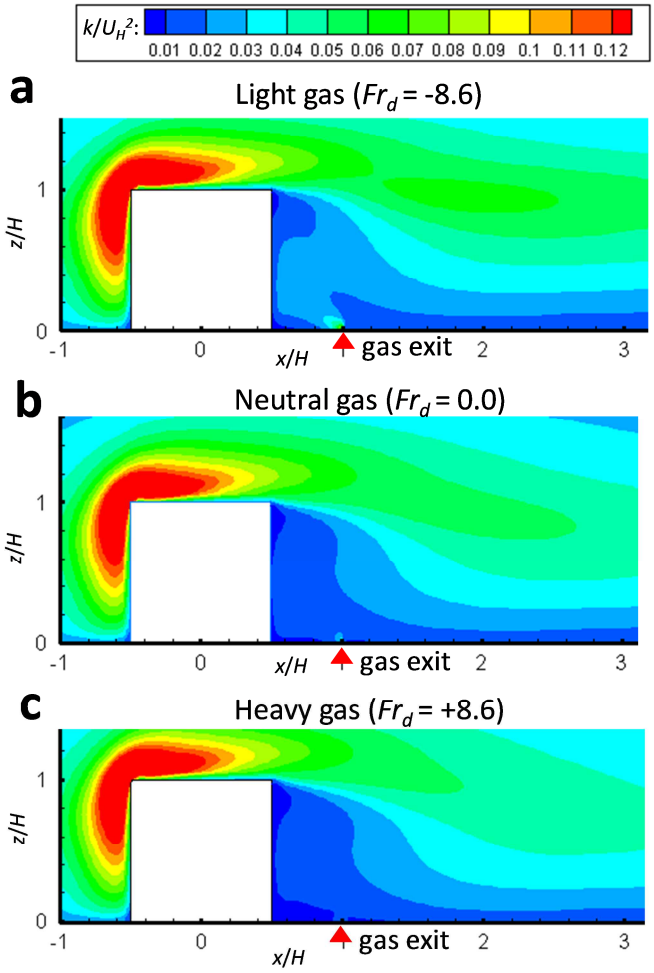

Figure 11. Contours of the turbulent kinetic energy k at the center section with different plume buoyancies: (a) light gas, (b) neutral gas, and (c) heavy gas.

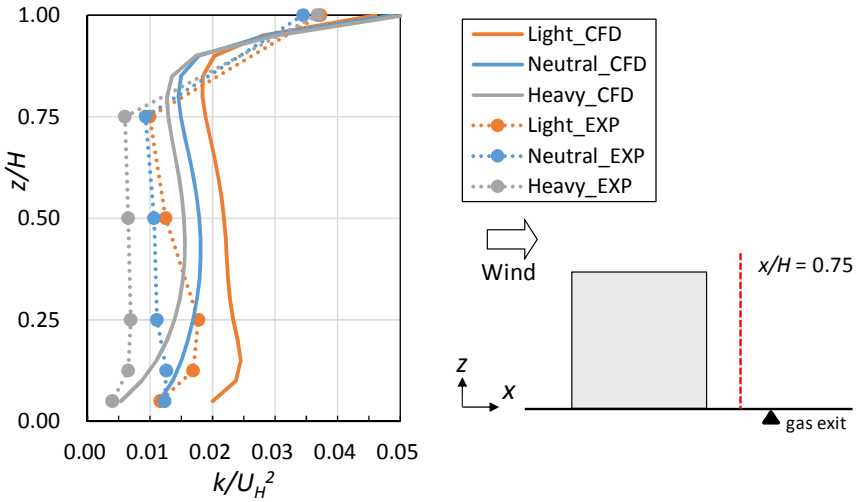

Figure 12. Vertical profiles of the turbulent kinetic energy k near the source position

5.2 Impact of the plume buoyancies on the concentration fields

Figure 13 illustrates the contours of the mean concentration at the center section obtained by CFD and the experiment for the different buoyant gas. The computational results are obtained with Sc_t =0.7 and without the buoyancy effect in the ε equation ($C_{3\varepsilon}$ = 0 in Eq. (8)). Note that the contour obtained by the experiment may be expressed differently from those obtained by the CFD models because the experimental measuring pitch is coarse, especially near the source. The general tendencies that the concentrations from the source exit are advected by the recirculation flow behind the building and that a high-concentration region appeared in the windward direction of the exit are well reproduced. For the light gas case, the experimental result implies that the concentration in the windward direction of the exit was lower than that for the neutral gas. Such a distribution is clearly affected by the positive buoyancy of the tracer gas. Although the computational results successfully reproduce the impact of buoyancy on the mean concentration distributions in the experimental results, the upward spreads of the concentrations are predicted to be generally smaller than those obtained by the experiment. In contrast to the result for the light gas, the experimental result for the heavy gas shows a very high concentration in the lower part of the wake region. This tendency is well reproduced in the CFD result. Figure 14 illustrates the iso-surfaces of the mean concentration C/C_0 = 2.5 predicted by CFD for different plume buoyancies. The volumes of the contaminated zone are quite different for the plume buoyancies (i.e., the high concentrations remained within the wake region for the light gas case and largely spread downwind for the heavy gas case). This tendency is consistent with the results obtained by the previous studies [21, 25, 28].

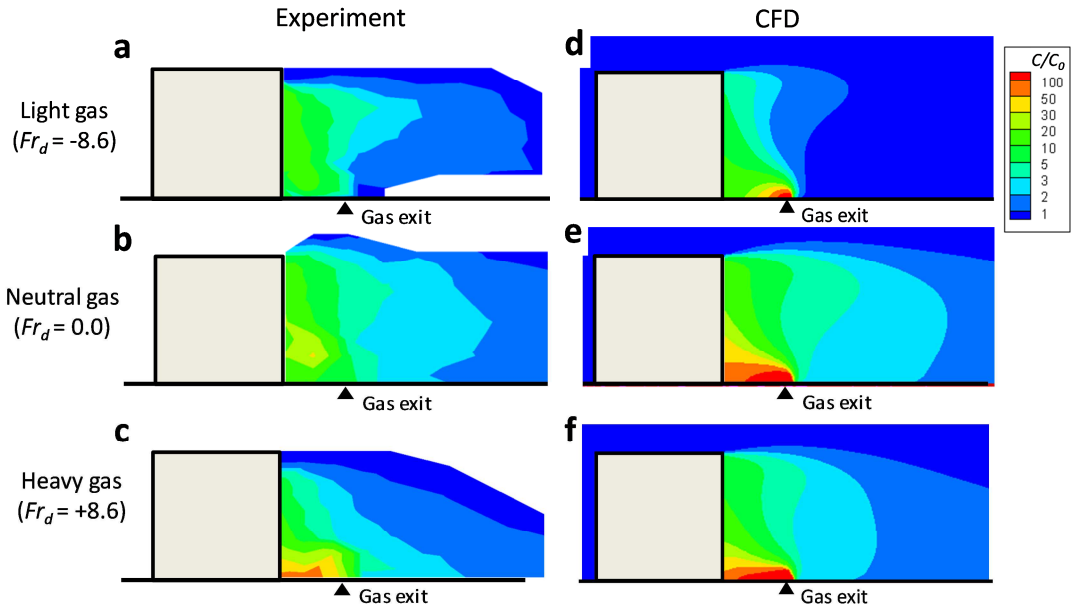

Figure 13. Contours of the mean concentrations C/C_0 at the center section with different plume buoyancies: (a–c) Experiment and (d–f) CFD.

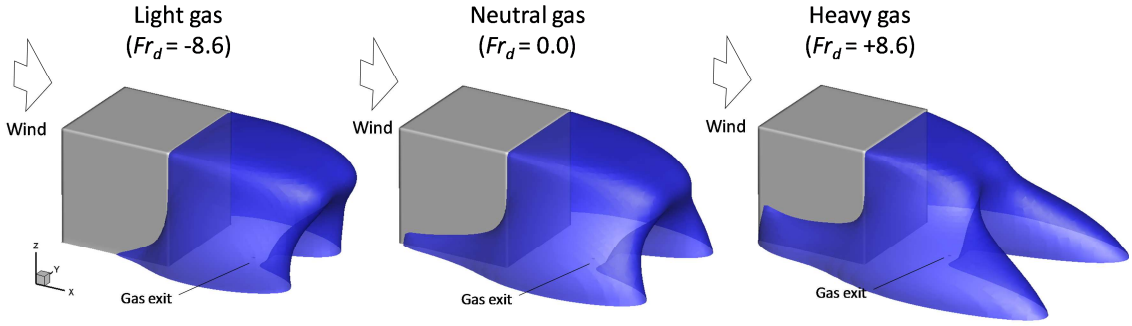

Figure 14. Iso-surfaces of the mean concentration C/C_0 = 2.5 predicted by the CFD for different plume buoyancies.

Figure 15 illustrates the vertical profiles at the center plane (y/H = 0) and the horizontal profiles at the half height of the building (z/H = 0.5) of the mean concentration behind the building for the light gas. The results obtained by modeling using different ε equations are also compared: without model, a model with Eq. (7) (Model 1), and a model with Eq. (8) (Model 2). The modeling using different ε equations almost has no effect on the predicted results. Although the overall concentration profiles are generally reproduced in the experimental results, all the

predicted concentrations are overestimated in the wake region behind the building. Especially, the rapid decrease in concentration just above the gas exit observed in the experiment (Fig. 15a) is not reproduced in the computation. This indicates that the diffusion effect in this region is underestimated in the predicted transport process of the concentrations for the light gas case.

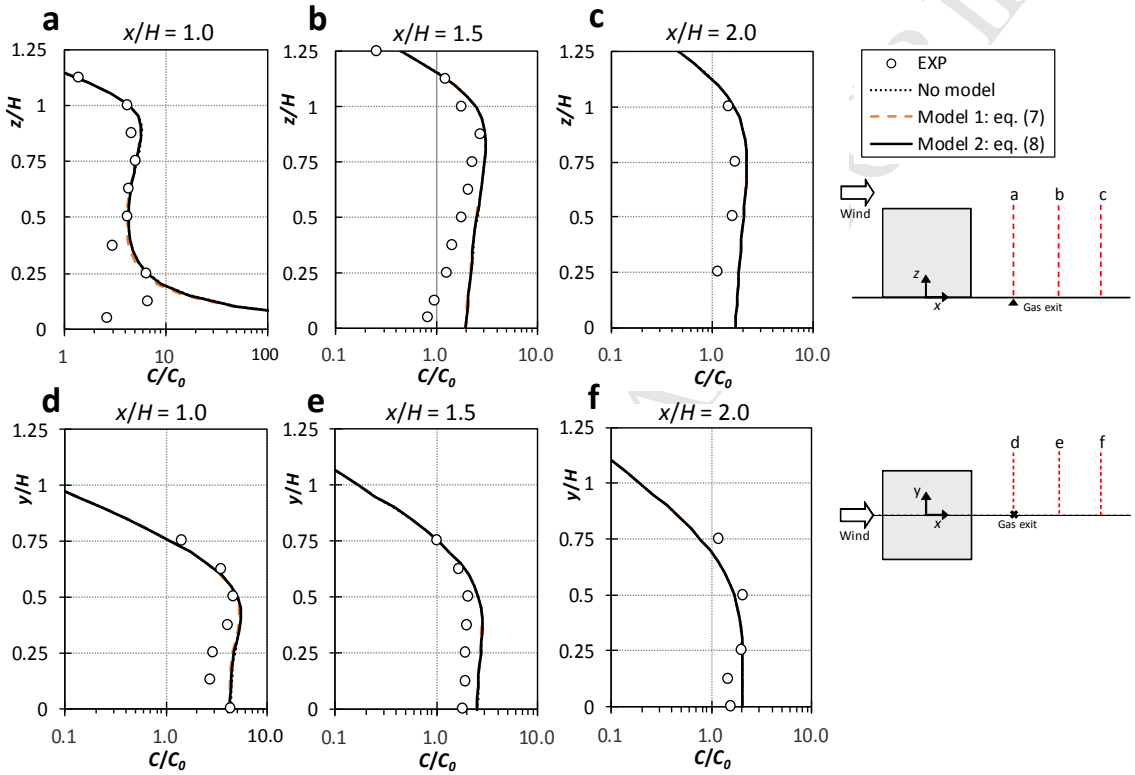

Figure 15. Profiles of the mean concentration C/C_0 behind the building for light gas: (a–c) Vertical profiles at the center section (y/H = 0) (d–f) horizontal profiles at a half building height (z/H = 0.5).

Figure 16 shows a comparison of the vertical and horizontal profiles of the mean concentration behind the building with the experimental data for the heavy gas case. The results for different modeling types for the buoyancy term in the ε equation are also compared. Although the impact of the buoyancy term is almost negligible, the model with Eq. (10) provides slightly better results than the other models. The predicted overall concentration profiles are generally reproduced in the experimental results. However, the concentrations are overestimated by CFD, especially outside the wake

region behind the building in the horizontal plane, in contrast to that for the light gas. That is, the diffusion effect is overestimated in the predicted transport process of the concentrations for the heavy gas case.

Table 3 lists the validation metrics for the light and heavy gases. The performance of the CFD predictions for the light gas is slightly poorer than for the neutral gas (Table 2) with FAC2 and FB. The model performance for the heavy gas is better than for the light gas, but slightly worse than for the neutral gas with FAC2 and FB. For buoyant gases, the values of NMSE are much larger than those of the neutral gas. Although a large value of NMSE implies that the predicted results scatter significantly from the observation results, the scatter plots (not shown here) indicate that the prediction results are systematically underestimated (overestimated) for the light (heavy) gases.

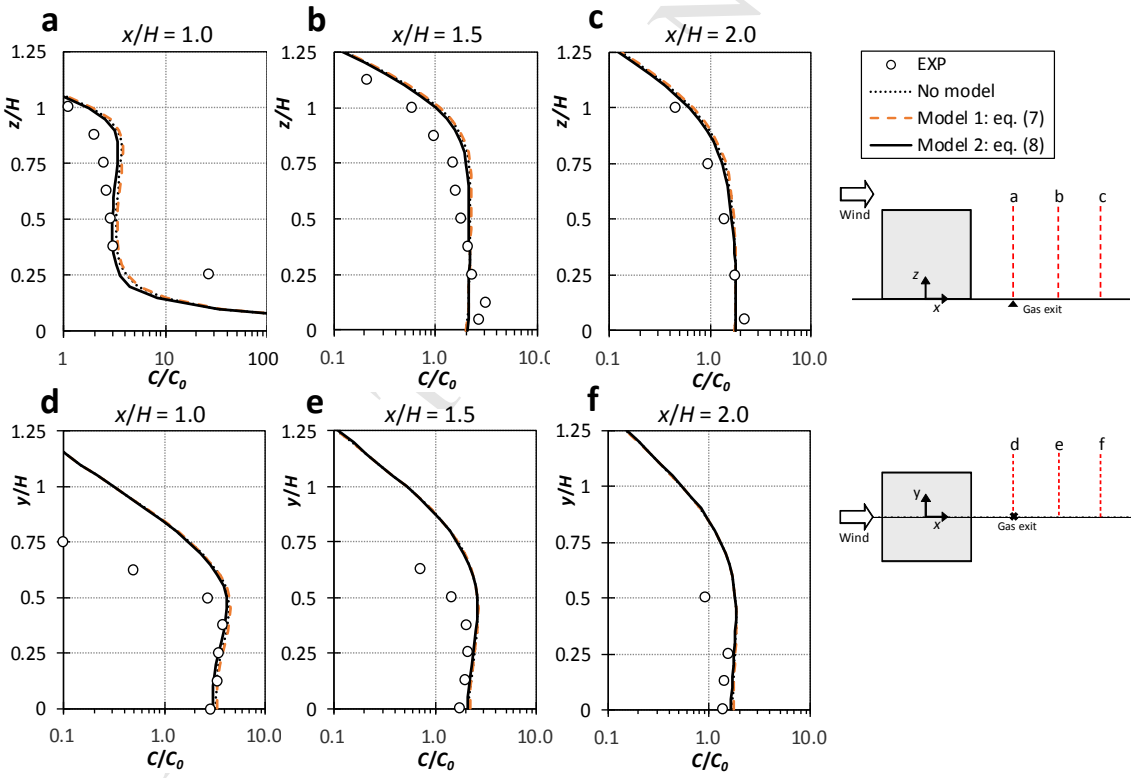

Figure 16. Profiles of the mean concentration C/C_0 behind the building for heavy gas: (a–c) Vertical profiles at the center section (y/H = 0) and (d–f) horizontal profiles at a half building height (z/H = 0.5).

Table 3. Validation metrics for the mean concentration C/C_0 for light and heavy gases.

	Buoyancy term in the ε equation	FAC2	FB	NMSE
Light gas (Fr_d = −8.6)	NA	0.83	−0.79	29.14
	Eq. (7)	0.84	−0.81	30.02
	Eq. (8)	0.83	−0.79	29.15
Heavy gas (Fr_d = +8.6)	NA	0.88	0.37	21.51
	Eq. (7)	0.88	0.35	20.95
	Eq. (8)	0.91	0.41	22.61

The cause of the prediction accuracy differences for the plume buoyancies can be interpreted as follows: Although the kinetic energy k values in the wake are overestimated by CFD for all the cases (see Figure 12), the diffusion effect of pollutant transport is underestimated, and therefore, the concentration is overestimated for light gas. The is because large-scale fluctuations behind the building that are not reproduced in the present steady RANS computations becomes apparent for the light gas where the plume strongly rises with positive buoyancy (see Figure 10) [16, 29]. On the other hand, for the heavy gases, the diffusion process (especially in the lateral direction) of pollutant transport is overestimated. This is mainly due to the overestimation of the turbulent kinetic energy in the wake region (Figure 11), even though the turbulence is suppressed by density stratification through turbulence modeling.

5.3 Impact of the turbulent Schmidt number on the prediction performance for different plume buoyancies

Figure 17 shows the variation in the validation metrics with different Sc_t values for different buoyant gases. For the neutral gas, the lower Sc_t values provide better results for all the metrics as mentioned in Section 4.3. This tendency is consistent with that observed in previous studies [51, 52]. For the light gas, all the metrics deteriorated drastically with the increase in Sc_t compared with those of the neutral gas. This implies that the facilitated turbulent diffusion due to positive buoyancy is not represented sufficiently by the present computational method, i.e., the Boussinesq approximation and the turbulence modeling of buoyancy. On the other hand, for the heavy gas, although the metrics are less sensitive to the value of Sc_t, the increase in Sc_t provides slightly better results. This is due to the non-apparent underestimation of the diffusion effect behind the building when using steady RANS simulations, because the diffusion

effect should be suppressed by the negative buoyancy. The optimum value of Sc_t was reported to increase with the increase of Richardson number, which expresses atmospheric stability, in a previous study [53]. Because most of the wake region is stable ($\frac{\partial \rho}{\partial z} < 0$) for the heavy gas, the present results are consistent with the previous findings. Furthermore, considering the good performance of CFD for the neutral gas, the relatively poor performance for the buoyant gases may be improved by modifying the modeling of G_b in the k equation (Eq. (7)) and the modeling of the turbulent scalar flux (Eq. (11)), which are based on the simple gradient diffusion hypothesis [54–56].

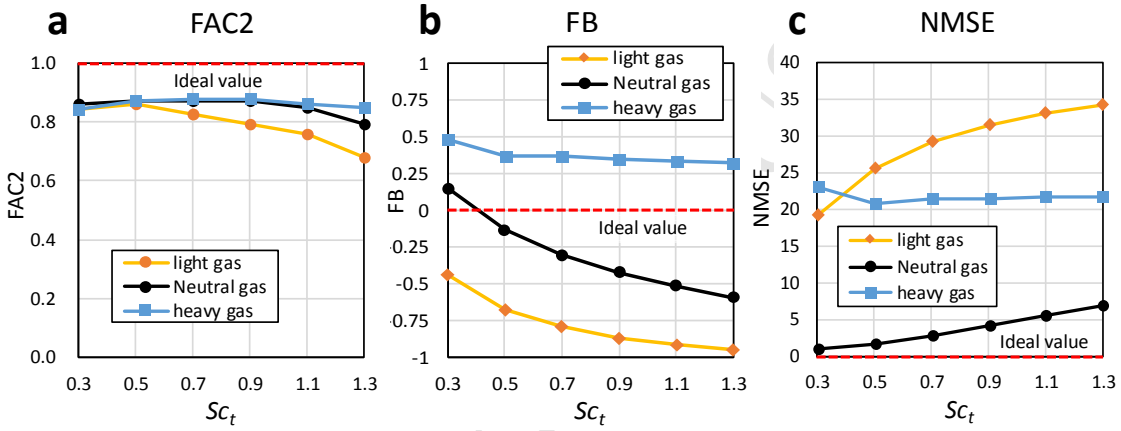

Figure 17. Sensitivity of the turbulent Schmidt number Sc_t to the validation metrics for different plume buoyancies: (a) FAC2, (b) FB, and (c) NMSE.

6. Conclusions

This study performed CFD simulations for flow and dispersion fields around a cubic building model with tracer gases of three different densities being exhausted from an exit behind the building. The following conclusions can be drawn from the results of this work:

- In the neutral gas case, the realizable k–ε model showed the best agreement with the experimental data in terms of the mean concentration distributions among the four different turbulence models (i.e., standard k–ε, RNG k–ε, realizable k–ε, and k–ω SST models).
- The steady RANS computations with the Boussineq approximation could reproduce the effect of the plume buoyancy on the mean concentration in the experimental results. Based on the reasonable agreement of the predicted results with the

experimental results, steady RANS computation with the Boussineq approximation can be a practical choice for this type of buoyant pollutant dispersion.

- The prediction performance for the light gas was slightly poorer than that for the neutral gas, and the prediction performance for the heavy gas was better than that for the light gas, but slightly worse than that for the neutral gas. However, the scattering of the predicted values from the experimental ones for the buoyant gases were much larger than those for the neutral gas.
- For the light gas, the CFD models overestimate the concentrations in the wake region, indicating that the effect of turbulent diffusion was underestimated. On the other hand, for the heavy gas, the CFD models overestimate the concentrations outside the wake region behind the building, indicating that the effect of turbulent diffusion was overestimated.
- This tendency was closely related with the prediction accuracy of the flow and turbulence fields behind the building, which is restricted by the steady RANS computations.
- For the buoyant gases, the buoyancy modeling in the ε equation showed a negligible influence on the results, especially for the light gas.
- The sensitivity of the turbulent Schmidt number to the prediction performance was examined for different buoyant gases. The prediction performance is more sensitive to the turbulent Schmidt number for the light gas case than the neutral gas, but less sensitive for the heavy gases.

A higher-order modeling of the turbulent scalar flux will be performed in a future research to clarify further the reason why the prediction performance of pollutant concentrations is poorer for buoyant gases than for neutral gas.

Acknowledgments

The authors would like to express their gratitude for the financial support provided to the first author through the Grants-in-Aid for Scientific Research in Japan (no. 16H04467). The authors also acknowledge Prof. Dr. S. Murakami, Prof. Dr. A. Mochida, and Ms. A. Shibuya, who supported the experiment in the Institute of Industrial Science, The University of Tokyo. The authors would also like to express

their sincere gratitude to the anonymous reviewers for their valuable comments and suggestions.

References

[1] Y. Tominaga, T. Stathopoulos, Ten questions concerning modeling of near-field pollutant dispersion in the built environment, Build. Environ. 105 (2016) 390–402.

[2] R.N. Meroney, Lift off of buoyant gas initially on the ground, J. Wind Eng. Ind. Aerodyn. 5 (1979) 1–11.

[3] P.T. Roberts, D.J. Hall, Wind tunnel simulation. Boundary layer effects in dense gas dispersion experiments, J. Loss Prev. Proc. Ind. 7(2) (1994) 106–117.

[4] W.H. Snyder, Similarity criteria for the application of fluid models to the study of air pollution meteorology, Bound -Lay. Meteorol. 3 (1) (1972) 113–134.

[5] S.P.S. Arya, J.F. Lape, Jr., A comparative study of the different criteria for the physical modeling of buoyant plume rise in a neutral atmosphere, Atmos. Environ. pt A. 24 (2) (1990) 289–295.

[6] A. Robins, I. Castro, P. Hyden, N. Steggel, D. Contini, D. Heist, T.J. Taylor, A wind tunnel study of dense gas dispersion in a stable boundary layer over a rough surface, Atmos. Environ. 35 (2001) 2253–2263.

[7] X.X. Li, C.H. Liu, D.Y.C. Leung, K.M. Lam, Recent progress in CFD modelling of wind field and pollutant transport in street canyons, Atmos. Environ. 40 (2006) 5640–5658.

[8] B. Blocken, T. Stathopoulos, J. Carmeliet, J.L.M. Hensen, Application of CFD in building performance simulation for the outdoor environment: An overview, J. Build. Perform. Simu. 4 (2011) 157–184.

[9] Y. Tominaga, T. Stathopoulos, CFD simulation of near-field pollutant dispersion in the urban environment: A review of current modeling techniques, Atmos. Environ. 79 (2013) 716–730.

[10] S. Di Sabatino, R. Buccolieri, P. Salizzoni, Recent advancements in numerical modelling of flow and dispersion in urban areas: A short review, Int. J. Environ. Pollut. 52(3/4) (2013) 172–191.

[11] B. Blocken, 50 years of computational wind engineering: Past, present and future, J. Wind Eng. Ind. Aerodyn. 129 (2014) 69–102.

[12] M. Lateb, R.N. Meroney, M. Yataghene, H. Fellouah, F. Saleh, M.C. Boufadel, On the use of numerical modelling for near-field pollutant dispersion in urban environments: A review, Environ. Pollut. 208 (Part A) (2016) 271–283.

[13] S. Di Sabatino, R. Buccolieri, B. Pulvirenti, R. Britter, Simulations of pollutant dispersion within idealised urban-type geometries using CFD and integral models, Atmos. Environ. 41 (2007) 8316–8329.

[14] B. Blocken, T. Stathopoulos, P. Saathoff, X. Wang, Numerical evaluation of pollutant dispersion in the built environment: Comparisons between models and experiments, J. Wind Eng. Ind. Aerodyn. 96 (2008) 1817–1831.

[15] Y. Tominaga, T. Stathopoulos, Numerical simulation of dispersion around an isolated cubic building: Comparison of various types of k-ε models, Atmos. Environ. 43 (20) (2009) 3200–3210.

[16] Y. Tominaga, T.Stathopoulos, Numerical simulation of dispersion around an isolated cubic building: Model evaluation of RANS and LES, Build. Environ. 45 (2010) 2231–2239.

[17] P. Gousseau, B. Blocken, T. Stathopoulos, G.J.F. van Heijst, CFD simulation of near-field pollutant dispersion on a high-resolution grid: A case study by LES and RANS for a building group in downtown Montreal, Atmos. Environ. 45(2) (2011) 428–438.

[18] M. Chavez, B. Hajra, T. Stathopoulos, A. Bahloul, Near-field pollutant dispersion in the built environment by CFD and wind tunnel simulations, J. Wind Eng. Ind. Aerodyn. 99 (2011) 330–339.

[19] A.O. Demuren, W. Rodi, Three-dimensional numerical calculations of flow and plume spreading past cooling towers, J. Heat Transfer, 109 (1987) 113–119.

[20] G.A. Perdikaris, F. Mayinger, Numerical simulation of the spreading of buoyant gases over topographically complex terrain, Int. J. Energ. Res. 18 (1994) 53–61

[21] H.A. Olvera, A.R. Choudhuri, W.-W. Li, Effects of plume buoyancy and momentum on the near-wake flow structure and dispersion behind an idealized building, J. Wind Eng. Ind. Aerodyn. 96(2) (2008) 209–228.

[22] L.H. Hu, Y. Xu, W. Zhu, L. Wu, F. Tang, K.H. Lu, Large eddy simulation of pollutant gas dispersion with buoyancy ejected from building into an urban street canyon, J. Hazard. Mater. 192 (3) (2011) 940–948.

[23] S.B. Sutton, H. Brandt, B.R. White, Atmospheric dispersion of a heavier-than-air gas near a two-dimensional obstacle, Bound.-Lay. Meteorol. 35 (1986) 125–153.

[24] F. Gavelli, E. Bullister, H. Kytomaa, Application of CFD (Fluent) to LNG spills into geometrically complex environments, J. Hazard. Mater. 159 (2008) 158–168.

[25] F. Scargiali, F. Grisafi, A. Busciglio, A. Brucato, Modeling and simulation of dense cloud dispersion in urban areas by means of computational fluid dynamics, J. Hazard. Mater. 197 (2011) 285–293.

[26] S.M.Tauseef, D. Rashtchian, S.A. Abbasi, CFD-based simulation of dense gas dispersion in presence of obstacles, J. Loss Prevent. Proc. 24(4) (2011) 371–376.

[27] R.N. Meroney, CFD modeling of dense gas cloud dispersion over irregular terrain, J. Wind Eng. Ind. Aerodyn. 104-106 (2012) 500–508.

[28] R. Ohba, A. Kouchi, T. Hara, V. Vieillard, D. Nedelka, Validation of heavy and light gas dispersion models for the safety analysis of LNG tank, J. Loss Prevent. Proc. 17 (2004) 325–337.

[29] Y. Tominaga, T. Stathopoulos, Steady and unsteady RANS simulations of pollutant dispersion around isolated cubical buildings: Effect of large-scale fluctuations on the concentration field, J. Wind Eng. Ind. Aerodyn. 165 (2017) 23–33.

[30] M. Schatzmann, A.J. Policastro, Effect of the Boussinesq approximation on the results of strongly-buoyant plume calculations. J. Climate Appl. Meteor. 23 (1) (1984) 117-123.

[31] M. Lateb, C. Masson, T. Stathopoulos, C. Bédard, Simulation of near-field dispersion of pollutants using detached-eddy simulation, Comput. Fluids 100 (2014) 308–320.

[32] Y. Tominaga, S. Murakami, A. Mochida, A. Shibuya, Y. Noguchi, Wind tunnel tests on turbulent diffusion and concentration fluctuation of buoyant gas near building, in: Proceedings of 12th National Symposium on Wind Engineering, 119–124, 1992. (in Japanese)

[33] Y. Tominaga, S. Murakami, A. Mochida, CFD prediction of gaseous diffusion around a cubic model using a dynamic mixed SGS model based on composite grid technique, J. Wind Eng. Ind. Aerodyn. 67&68 (1997) 827–841.

[34] Ansys Fluent 16.0 Theory Guide, Ansys Inc., Canonsburg, U.S.A., 2014.

[35] P.F. Crapper, W.D. Baines, Some remarks on non-boussinesq forced plumes, Atmos. Environ. 12 (10) (1978) 1939-1941.

[36] P.F. Crapper, W.D. Baines, Non boussinesq forced plumes, Atmos. Environ. 11 (5) (1977), 415–420.

[37] S.V. Patankar, D.B. Spalding, A calculation procedure for heat, mass and momentum transfer in three-dimensional parabolic flows, Int. J. Heat Mass Trans. 15 (10) (1972) 1787–806.

[38] J. Franke, A. Hellsten, H. Schlünzen, B. Carissimo, Best practice guideline for the CFD simulation of flows in the urban environment, COST Office, Brussels, 2007.

[39] Y. Tominaga, A. Mochida, R. Yoshie, H. Kataoka, T. Nozu, M. Yoshikawa, T. Shirasawa, AIJ guidelines for practical applications of CFD to pedestrian wind environment around buildings, J. Wind Eng. Ind. Aerodyn. 96 (2008) 1749–1761.

[40] B. Blocken, T. Stathopoulos, J. Carmeliet, CFD simulation of the atmospheric boundary layer: wall function problems, Atmos. Environ. 41 (2007) 238–252.

[41] B.E. Launder, D.B. Spalding, Mathematical models of turbulence, Academic Press, New York, U.S.A., 1972.

[42] V. Yakhot, S.A. Orszag, S. Thangam, T.B. Gatski, C.G. Speziale, Development of turbulence models for shear flows by a double expansion technique, Phys. Fluids A 4 (1992) 1510–1520.

[43] T.H. Shih, W.W. Liou, A. Shabbir, Z. Yang, J. Zhu, A new k-ε eddy viscosity model for high Reynolds number turbulent flows, Comput. Fluids 24 (1995) 227–238.

[44] F.R. Menter, Two-equation eddy-viscosity turbulence models for engineering applications, AIAA J. 32 (1994) 1598–1605.

[45] R. Kumar, A. Dewan, Computational models for turbulent thermal plumes: Recent advances and challenges, Heat Transfer Eng. 35 (4) (2014) 367–383.

[46] P.L. Viollet, The modelling of turbulent recirculating flows for the purpose of reactor thermal-hydraulic analysis, Nucl. Eng. Des. 99 (1987) 365–377.

[47] Y. Tominaga, T. Stathopoulos, Turbulent Schmidt numbers for CFD analysis with various types of flowfield, Atmos. Environ. 41(37) (2007) 8091–8099.

[48] M. Schatzmann, H. Olesen, J. Franke (Eds.), COST 732 Model Evaluation Case Studies: Approach and Results, University of Hamburg, Hamburg, Germany, 2010.

[49] S.R. Hanna, O.R. Hansen, S. Dharmavaram, FLACS CFD air quality model performance evaluation with Kit Fox, MUST, Prairie Grass, and EMU observations, Atmos. Environ. 38 (2004) 4675–4687.

[50] Y. Tominaga, A. Mochida, S. Murakami, S. Sawaki, Comparison of various revised k-ε models and LES applied to flow around a high-rise building model with 1:1:2 shape placed within the surface boundary layer, J. Wind Eng. Ind. Aerodyn. 96 (2008) 389–411.

[51] P. Gousseau, B. Blocken, G.J.F. van Heijst, CFD simulation of pollutant dispersion around isolated buildings: On the role of convective and turbulent mass fluxes in the prediction accuracy, J. Hazard. Mater. 194 (2011) 422–434.

[52] B. Blocken, R. Vervoort, T. van Hooff, Reduction of outdoor particulate matter concentrations by local removal in semi-enclosed parking garages: A preliminary case study for Eindhoven city center, J. Wind Eng. Ind. Aerodyn. 159 (2016) 80–98.

[53] M.R. Mokhtarzadeh-Dehghan, A. Akcayoglu, A.G. Robins, Numerical study and comparison with experiment of dispersion of a heavier-than-air gas in a simulated neutral atmospheric boundary layer, J. Wind Eng. Ind. Aerodyn. 110 (2012) 10–24.

[54] B.J. Daly, F.H. Harlow, Transport equations in turbulence, Phys. Fluids 13 (1970) 2634–2649.

[55] M.M. Gibson, B.E. Launder, Ground effects on pressure fluctuations in the atmospheric boundary layer, J. Fluid Mech. 86 (3) (1978) 491–511.

[56] K. Van Maele, B. Merci, Application of two buoyancy-modified k-epsilon turbulence models to different types of buoyant plumes, Fire Safety J. 41 (2) (2006) 122–138.

Highlights

- Steady RANS simulations for dispersion with plume buoyancies were performed.
- The model performance was examined by comparing the results with experimental results.
- CFD generally reproduced the impact of plume buoyancies on the mean concentration.
- The model performance was affected by the prediction accuracy of the flow field.